Real-time imaging of optic nerve head collagen microstructure and biomechanics using instant polarized light microscopy

Po-Yi Lee[1,2], Bin Yang[3], Yi Hua[2], Susannah Waxman[2],
Ziyi Zhu[1,2], Fengting Ji[1,2], Ian A Sigal[1,2*]

[1] Department of Bioengineering, Swanson School of Engineering,
[2] Department of Ophthalmology, School of Medicine,
University of Pittsburgh, Pittsburgh, PA
[3] Department of Engineering, Rangos School of Health Sciences,
Duquesne University, Pittsburgh, PA

Short Title: Imaging ONH micromechanics in real time

* Correspondence:
Ian A. Sigal, Ph.D.
Laboratory of Ocular Biomechanics
Department of Ophthalmology, University of Pittsburgh School of Medicine
203 Lothrop Street, Eye and Ear Institute, Room 930, Pittsburgh, PA 15213
Phone: (412) 864-2220; Fax: (412) 647-5880
Email: ian@OcularBiomechanics.com
www.OcularBiomechanics.com

Key Words: polarized light microscopy; optic nerve head; collagen; crimp; deformation; Lamina cribrosa

Disclosures: Ziyi Zhu was at the University of Pittsburgh when he contributed to this work. He is now at Amazon; Other authors have nothing to disclose.

1   **Highlights**

2   • We demonstrate that instant polarized light microscopy allows visualization and
3   quantification of changes in optic nerve head collagen morphology and architecture under
4   dynamic loading

5   • We show crimped collagen fibers in the peripapillary sclera and lamina cribrosa
6   straightening under load, without torsion and with only small rotations.

7   • We show that stretch-induced local deformation of the peripapillary sclera was nonlinear
8   and nonaffine.

9   • We show that stretch-induced lamina cribrosa pore deformation was anisotropic and
10   heterogeneous among pores.

11   • Our results show this novel imaging technique could help understand the role of collagen
12   microstructure in eye physiology, aging, and in biomechanics-related diseases, such as
13   glaucoma and myopia.

14

15 **Abstract**

16

17   Current tools lack the temporal or spatial resolution necessary to image many important

18   aspects of the architecture and dynamics of the optic nerve head (ONH). We evaluated the

19   potential of instant polarized light microscopy (IPOL) to overcome these limitations by leveraging

20   the ability to capture collagen fiber orientation and density in a single image. Coronal sections

21   through the ONH of fresh normal sheep eyes were imaged using IPOL while they were stretched

22   using custom uniaxial or biaxial micro-stretch devices. IPOL allows identifying ONH collagen

23   architectural details, such as fiber interweaving and crimp, and has high temporal resolution,

24   limited only by the frame rate of the camera. Local collagen fiber orientations and deformations

25   were quantified using color analysis and image tracking techniques. We quantified stretch-

26   induced collagen uncrimping of lamina cribrosa (LC) and peripapillary sclera (PPS), and changes

27   in LC pore size (area) and shape (convexity and aspect ratio). The simultaneous high spatial and

28   temporal resolutions of IPOL revealed complex ONH biomechanics: i) stretch-induced local

29   deformation of the PPS was nonlinear and nonaffine. ii) under load the crimped collagen fibers in

30   the PPS and LC straightened, without torsion and with only small rotations. iii) stretch-induced LC

31   pore deformation was anisotropic and heterogeneous among pores. Overall, with stretch the

32   pores were became larger, more convex, and more circular. We have demonstrated that IPOL

33   reveals details of collagen morphology and mechanics under dynamic loading previously out of

34   reach. IPOL can detect stretch-induced collagen uncrimping and other elements of the tissue

35   nonlinear mechanical behavior. IPOL showed changes in pore morphology and collagen

36   architecture that will help improve understanding of how LC tissue responds to load.

37

1. Introduction

Collagen fibers are a primary load-bearing component of the optic nerve head (ONH), and thus their organization and behavior under load play a central role in the physiology and pathophysiology of the eye. (Coudrillier et al., 2012; Ethier et al., 2004a) Many imaging techniques have been deployed for measuring and/or visualizing the architecture and biomechanics of ONH collagen. These include confocal, (Kang and Yu, 2015; Masters, 1998) nonlinear, (Behkam et al., 2019; Brown et al., 2007; Sigal et al., 2014a) scanning electron, (Quantock et al., 2015; Quigley and Addicks, 1981; Quigley et al., 1983) and transmission electron (Elkington et al., 1990) microscopies, small-angle light scattering, (Girard et al., 2011; Yan et al., 2011) electronic speckle pattern interferometry, (Bianco et al., 2020; Girard et al., 2009) magnetic resonance imaging, (Ho et al., 2014; Ho et al., 2016) ultrasound, (Ma et al., 2020; Ma et al., 2019; Pavlatos et al., 2018; Pavlatos et al., 2016; Qian et al., 2020) and optical coherence tomography. (Fazio et al., 2018; Midgett et al., 2019) Each of these techniques offers a unique combination of resolution, field of view, penetration depth, speed, and tissue specificity. For instance, nonlinear microscopy has high tissue specificity and spatial resolution, but it has low imaging speed and a small field of view. Thus, studies of ONH biomechanics using nonlinear microscopy have been limited to static or quasi-static conditions. (Sigal et al., 2014a) Electronic speckle pattern interferometry allows real-time imaging, and has excellent resolution to resolve sub-fiber level deformations, but does not discern collagen and has extremely low penetration into tissues. (Bianco et al., 2020) Optical coherence tomography works well in-vivo and has therefore been widely deployed for both research (Sigal et al., 2014b) and clinical (Schuman et al., 2020) work. However, its limitations, primarily in resolution and signal penetration, have precluded its use to quantify local ONH tissue architecture and biomechanics.

Over the past several years, polarized light microscopy (PLM) has been demonstrated to allow visualization and quantification of ONH collagen tissues with micrometer-scale resolution over wide regions. (Brazile et al., 2018; Gogola et al., 2018a; Gogola et al., 2018b; Jan et al., 2018; Jan et al., 2017a; Jan and Sigal, 2018; Jan et al., 2015; Jan et al., 2017b; Yang et al., 2018a; Yang et al., 2018b) PLM has proven extremely useful for the study of tissues ex vivo, revealing patterns of fiber architecture throughout the globes of humans and other animals. Importantly, the high angular resolution of PLM allows measurement of the degree of stretch or relaxation of collagen fibers, also referred to as crimp, that eludes other imaging techniques. Conventional PLM, however, requires multiple images acquired under various polarization states – four in our implementation. This slows down imaging, requires post-processing, such as image alignment, that affects image quality, and takes time. Hence, our studies using PLM were limited to static

72   evaluation of tissues from eyes fixed at different intraocular pressures (IOPs). This was

73   particularly limiting for the study of collagen fibers of lamina cribrosa (LC) beams, which vary so

74   substantially even between contralateral eyes.

75   Recently we introduced instant polarized light microscopy (IPOL), a variation of PLM, which

76   allows quantitative imaging of collagen at the full acquisition speed of the camera, with excellent

77   spatial and angular resolutions. (Lee et al., 2019a; Yang et al., 2019) Our goal was to demonstrate

78   IPOL for the quantitative analysis of both architecture and dynamics of ONH collagen. Specifically,

79   we set out to visualize and quantify the microstructure and real-time dynamic response to stretch

80   of collagen fibers of the peripapillary sclera (PPS) and LC. We give several examples that illustrate

81   the great potential that dynamic visualization and quantification of the PPS and LC collagen with

82   IPOL holds to help gain a better understanding of eye biomechanics and its role in health and

83   disease.

2. Methods

This section is organized into three parts. First, we introduce IPOL imaging and how the technique produces true-color images indicating collagen fiber orientation. Second, we describe how to calibrate the color-angle mapping by imaging a section of chicken Achilles tendon at known orientations. Chicken tendon was chosen for its highly ordered and simple – compared with the eye – collagen fiber organization. (Jan et al., 2015; Yang et al., 2018b) Third, we utilized IPOL to image the ONH collagen architecture and illustrate the potential of the technique. We do this using fresh sheep eyes and a series of uniaxial and biaxial tests. Uniaxial stretch was applied to visualize continuous tissue deformations in a small region. Uniaxial stretch is a fairly common technique when evaluating the mechanical behavior of highly anisotropic materials, such as tendon. (York et al., 2014) Biaxial stretch was applied to visualize quasi-static deformations of the entire ONH region. Biaxial stretch is useful to reveal collagen fiber realignment, including rotation and torsion, and is a better approximation to the physiologic loading of scleral tissue. (Chung et al., 2016) From the IPOL images we analyzed stretch-induced collagen deformation and uncrimping in the PPS and LC, and changes in LC pore morphology as illustrative of the multitude of microarchitecture data available from IPOL. The rationale and implications of our choices of illustrative examples and testing techniques are addressed in more detail in the Discussion.

2.1 IPOL imaging system

IPOL was implemented with a commercial inverted microscope (IX83; Olympus, Tokyo, Japan), as previously described. (Lee et al., 2019b; Yang et al., 2019; Yang et al., 2021) Briefly, a broadband white-light source, a set of polarization encoder and decoder (each consisting of a polarizer and a polarization rotator), and a color camera (acA1920-155uc, Basler AG, Ahrensburg, Germany) were used in this system. In the absence of a birefringent sample, the white light was blocked and the image background appeared dark (Figure 1a). With a birefringent sample, such as collagen, the spectrum of the white light was changed and the light appeared colorful (Figure 1b). The colorful light was acquired by a color camera to produce the true-color images indicating collagen fiber orientation (Figure 1c). The frame rate of IPOL was limited only by that of the color camera, which in our setup was 156 frames per second. The high-speed imaging performance of IPOL allows capturing stretch-induced tissue deformation in real time, which is essential in characterizing tissue mechanics. (Ethier et al., 2004b)

2.2 System calibration

114

Sample preparation. A chicken Achilles tendon was dissected and fixed with 10% formalin for 24 hours while under load to remove the natural undulations of collagen fibers, or crimp. (Yang et al., 2018b) Following fixation, the tendon was cryo-sectioned longitudinally into 30-μm-thick sections.

Color-angle mapping. IPOL images were acquired with the chicken tendon section at several controlled angles relative to the longitudinal fiber direction, from 0 to 90 degrees, every 2 degrees. The individual images were then registered using Fiji software. (Schindelin et al., 2012) A region of interest (ROI) on the tissue was manually selected on the stack, and the hue of the ROI was extracted by converting RGB (Red, Green, Blue) images into HSV (Hue, Saturation, Value) images. A color-angle conversion map was then computed by a circular interpolation of the measured hue and its corresponding orientation angle. The fiber orientation map for all images was then obtained by searching hue value over the color-angle conversion map for corresponding angles for all pixels (Figure 2).

2.3 Imaging ONH collagen architecture and deformation

Sample preparation. Normal sheep eyes about a year old were procured from a local abattoir within four hours after death. The muscles, fat, and episcleral tissues were carefully removed. The ONH region was isolated using an 11-mm-diameter trephine and embedded in optimum cutting temperature (OCT) compound (Tissue-Plus; Fisher Healthcare, TX, USA). Samples were then snap frozen in liquid nitrogen-cooled isopentane and sectioned coronally at a thickness of 16 μm. OCT was washed with multiple PBS baths. To prevent curling or tears at the clamp points, a tissue section was sandwiched between two pieces of silicone sheet (Medical Grade, 0.005"; BioPlexus, AZ, USA). The sheets also allowed using PBS to maintain tissue hydration without lensing.

ONH collagen architecture. Tissue samples were imaged using a 4x objective (numerical aperture [NA], 0.13). Due to the limited field of view of the objective, the image of the whole section was acquired using mosaicking. The mosaics were obtained with 20% overlap and stitched using Fiji. (Schindelin et al., 2012) We have previously shown that the visualization of collagen fibers is not affected by mosaics or stitching. (Jan et al., 2018; Jan et al., 2015)

Uniaxial stretch testing. For uniaxial testing, sections were mounted to a commercial uniaxial stretching device using custom-made clamps (Microvice; S.T. Japan, FL, USA). The clamps allowed us to set the sample at the focal plane of our optical system, which was different from the

146 commercial device default axis. The stretching process was imaged using IPOL in real-time
147 display mode (156 frames per second) with a 10x strain-free objective (NA, 0.3). For each testing,
148 either the LC or the PPS region was imaged. Our measurements were:

- 149 • *Maximum principal strain in the PPS.* Maximum principal strain was used to analyze
150 the local deformation of the PPS. A digital image correlation technique was used to
151 quantify the tissue displacement, and the maximum principal strain (a measure of
152 tensile strain) was then calculated as described elsewhere. (Wei et al., 2018)

- 153 • Orientation profile *of LC beams.* The change in fiber orientation profile determines the
154 crimp geometry of the collagen. The fiber orientation profiles along a beam were
155 measured with stretch. The crimp tortuosity of LC beams was then calculated as
156 previously described. (Brazile et al., 2018; Jan et al., 2018)

157 *Biaxial stretch testing.* Biaxial stretch testing is used to simultaneously extend the entire ONH
158 region equally along two axes, which is a better mimic of the in vivo inflation conditions than
159 uniaxial loading. Each section was mounted to a custom biaxial stretching device and then
160 stretched quasi statically (small stretch steps [<0.1%] followed by long (20s or more) pauses to
161 allow dissipating viscoelastic effects).(Lee et al., 2019a) At each step, multiple images were
162 captured to cover the entire ONH region in a mosaic. The section was imaged using IPOL with a
163 4x strain-free objective (NA, 0.13). Our measurements were:

- 164 • *Angle distribution in the PPS.* Changes in crimp are central to the nonlinear behavior
165 of the tissues. The changes in angle distribution along a bundle indicate if the loading
166 causes bundle rotation or torsion. Angles within a PPS region were extracted at the
167 initial and stretched states. We then used the Epanechnikov kernel to fit the angle
168 distribution at each state. (Bowman and Azzalini, 1997)

- 169 • *LC beam width.* The test determines if the change in LC beam width under the stretch
170 is related to crimp tortuosity of LC beams. We evaluated LC beam brightness profile
171 across three beams and then estimated the beam widths using the full-width at half-
172 maximum (FWHM). (Weik, 2001)

- 173 • *LC pore geometry.* Changes in LC pore geometry determines if LC pore deformation
174 was isotropic. We traced 17 LC pores at the initial and stretched states, and then
175 overlapped them to visualize pore deformation. Pore size (area) and shape (convexity
176 and aspect ratio) were measured, (Voorhees et al., 2017a) and a paired *t*-test was
177 used to evaluate their differences between the initial and stretched states. We used α
178 = 0.05 to establish significance.

3. Results

3.1 ONH collagen architecture

Figure 3 shows an example IPOL image mosaic acquired of a static coronal section through the ONH of a fresh sheep eye. The image illustrates the high spatial and angular resolutions of IPOL, which allow identification of several aspects of collagen architecture simultaneously. At the smaller scale, crimp, or the natural waviness of collagen fibers, is discernible in both the PPS and LC regions. At the medium scale we can recognize the LC beams, and the width and orientation of fiber bundles. The larger scale we discern the overall shape of the scleral canal and the general organization of collagen in the PPS.

3.2 Uniaxial stretch testing

Figure 4 illustrates local nonlinear deformations in a sample of PPS under uniaxial stretch visible using IPOL (Figure 4a). Tracking the fibers under stretch revealed that motion trails that were non-monotonic, inhomogeneous, tortuous and anisotropic (Figure 4b). A contour plot of the maximum principal strain shows that stretch-induced PPS deformation was non-affine, *i.e.*, the local deformation differs from the applied stretch. (Figure 4c).

The uncrimping process of an LC beam under uniaxial stretch is shown in Figure 5. Before stretch, a beam exhibits collagen fiber undulations (Figure 5a t = 0 ms). The undulations are discernible both based on the fiber edges and by the color bands. The crimp bands are perpendicular to the principal beam axis. Elsewhere we had speculated that these properties would cause the beam to stretch without torsion.(Jan et al., 2017a) As the beam was stretched, the undulations decreased, according to the expected collagen uncrimping (Figure 5a, t = 400 ms to t = 1200 ms). Taking advantage of IPOL quantitative information on the local fiber orientation, we plotted the orientations along a line along the beam axis (Figure 5b). The plot illustrates the regular sinusoidal nature of the crimp. The amplitude of the fiber orientation profile along the beam decreased as the stretch increased, another indication of collagen uncrimping. Interestingly, the uncrimping is not associated with a discernible increase in crimp period. This is consistent with our measurements in sclera and can be understood given the small undulation angles. (Jan and Sigal, 2018) Interestingly, the largest undulations uncrimped earlier in the stretch, such that the crimp was smaller and more uniform after stretch than before stretch. The uncrimping process can be further quantified by calculating the tortuosity as a function of time, which can potentially be used as input for constitutive model (Figure 5c). (Grytz and Meschke, 2009; Hill et al., 2012)

210   **3.3 Biaxial stretch testing**

211   Deformations of the PPS and LC under biaxial stretch are shown in Figure 6. In the PPS, the

212   angle distribution changed from bimodal at the initial state, indicating crimped fibers, into unimodal

213   at the stretched state (Figure 6a). The peak angle after stretch is not within the two initial peaks,

214   indicating that the uncrimping also involved a rotation of the fiber bundle. In the LC, crimp

215   tortuosity and beam decreased under the stretch (Figure 6b). However, we also noticed

216   something interesting worth pointing out: the beam with the least crimped collagen at the initial

217   state narrowed the most at the stretched state.

218   Figure 7 shows an example of analysis of stretch-related LC biomechanics at the pore level.

219   Comparing pores before and after stretch revealed that stretch-induced pore deformation was

220   anisotropic within a single pore and non-uniform among pores. Pores became larger, more

221   convex, and more circular after stretch (P's < 0.005).

4. Discussion

Our results demonstrate that IPOL is well-suited for the imaging and quantitative study of the architecture and dynamics of ONH collagen. Using IPOL we made several interesting observations. First, stretch-induced PPS deformation was non-affine, non-linear and non-uniform. Second, the crimped collagen fibers in the PPS and LC straightened under stretch, without torsion. Third, stretch-induced LC pore deformation was anisotropic within a single pore and non-uniform among pores. Below we discuss each of these observations and their implications in ONH biomechanics.

We observed that the distribution of strains in the PPS under uniaxial stretch was non-uniform. The highest strains were mainly located at fiber bundles oriented transversely to the stretch direction. Compared to bundles along the stretch direction, transverse bundles are less efficient at carrying the loads, and thus experienced higher strains perpendicular to the fiber orientations. In addition, the stretch-induced PPS deformation was non-affine. This raises the possibility of complex modes of energy storage and dissipation. (Billiar and Sacks, 1997) A common assumption of numerical models of the PPS, and many other soft tissues, is that the microstructure undergoes affine deformations. (Coudrillier et al., 2013; Girard et al., 2009; Grytz et al., 2012; Voorhees et al., 2018) If our observations under uniaxial stretch carryover to the physiologic conditions, it would indicate a fundamental limitation of current models and the need for more complex models that can account for non-affine fiber behavior. (Wang et al., 2020)

We observed that the crimped collagen fibers in the PPS and LC straightened under stretch. This phenomenon is well recognized in other tissues, like tendon and ligament, (Hansen et al., 2002; Thornton et al., 2002) We have also imaged and characterized collagen crimp and recruitment in ONH tissues, but the PLM techniques available required us to do it in samples fixed under different conditions. (Jan and Sigal, 2018) To the best of our knowledge, this study is the first showing the uncrimping process of ONH collagen under stretch. The process we report is consistent with theory of collagen fiber recruitment in soft tissues, in which fibers straighten with stretch to become straight are considered recruited, contributing to the local stiffening of the tissue. (Grytz and Meschke, 2009; Hill et al., 2012; Holzapfel, 2001) Collagen uncrimping and recruitment is an essential mechanism in the mechanical response of the eye tissues to mechanical load and deformation. Hence, the ability to visualize and quantify crimp under dynamic tests that IPOL provides represents a powerful opportunity to characterize and understand the tissues, and how the tissue behavior arises from collagen microarchitecture and

254 overall morphology. (Eilaghi et al., 2010; Girard et al., 2009; Jan and Sigal, 2018; Perez et al.,
255 2014)

256   Our results suggest that stretch-induced changes in an LC beam width may be related to its
257 microstructural crimp characteristics. Specifically, less crimped LC beams narrowed more under
258 stretch (a Poisson effect). This may affect the adjacent neural tissues due to the lateral movement
259 of the beam edges, and may cause increased stress within the beam due to decreased cross-
260 sectional area. Further work is needed to examine the spatial relationship between collagen crimp
261 in the LC and stretch-induced LC beam narrowing.

262   Analyzing stretch-induced LC pore deformation is critical to understand the biomechanical
263 insult to the neural tissues and vessels within the pores resulting from IOP. (Ling et al., 2019;
264 Sigal et al., 2007; Sigal et al., 2014a; Voorhees et al., 2017a; Voorhees et al., 2017b) Using IPOL,
265 we observed that stretch-induced LC pore deformation was anisotropic within a single pore and
266 non-uniform among pores. This indicates that neural tissues and vessels within LC pores may
267 experience multiple modes of deformation under stretch, such as stretch, compression, and
268 shear. Quantitative analysis further shows that pores became larger, more convex, and more
269 circular after stretch. This is consistent with numerical findings of IOP-induced changes in LC pore
270 morphology. (Voorhees et al., 2017a) Understanding how stretch influences pore deformation will
271 help clarify the association between the distribution of lamina pore shape and glaucoma status or
272 progress, which remains controversial in the literature. (Akagi et al., 2012; Fontana et al., 1998;
273 Miller and Quigley, 1988; Wang et al., 2013; Zwillinger et al., 2016) Of course, it is essential to
274 consider the conditions in which we did the experiments and the limitations these imply. We
275 discuss these further down.

276   The IPOL imaging technique, in which a single snapshot image encodes information of fiber
277 orientation and density, is uniquely well-suited to understanding the ONH collagen architecture
278 and behavior under dynamic loading. IPOL provides high spatial and angular resolutions, which
279 allows identifying collagen architectural details, such as fiber interweaving and crimp. Although
280 conventional PLM can also identify these details, its resolution is lower (Figure 8). PLM requires
281 post-processing (*i.e.*, image registration and denoising) multiple images to derive information such
282 as fiber orientation, which reduces the spatial detail of the image. IPOL also has high temporal
283 resolution, limited only by the frame rate of the camera. Hence, IPOL is suited for imaging
284 continuous tissue deformation under dynamic loading. Conventional PLM can only be employed
285 to image quasi-static tissue deformation, in which the dynamic process has to be split into multiple
286 static steps. (Tower et al., 2002) There are alternative faster PLM techniques, for example using
287 multiplexed analyzer filters, but these reduce the resolution. (Gruev et al., 2010)

288   It is important to consider the limitations of IPOL and our analysis in this work. First, we used
289   sheep eyes to study the ONH collagen deformation under stretch. Sheep eyes are similar to
290   human eyes in that they have a collagenous LC, but differ in having a ventral groove in the ONH,
291   similar to that in pig. (Brooks et al., 1998) Though it is possible that stretch-induced ONH collagen
292   deformation found in sheep is not the same in humans, it is important to understand sheep as an
293   animal model. (Candia et al., 2014; Gerometta et al., 2010) Future work should include additional
294   animal models as well as human eyes. The sheep from which we obtained the eyes were young,
295   as is to be expected from an abattoir. We have shown that crimp in the eye decreases with age,
296   (Gogola et al., 2018a) and thus it is possible that older eyes behave differently.

297   Second, IPOL is based on transmitted light illumination, which requires the tissue samples to
298   be cut into fairly thin sections (thickness of 16 μm in this study). Thus, while the architecture of
299   collagen fibers in the samples is three-dimensional, we have limited the sample to a two-
300   dimensional "slab". Although some publications have obtained valuable information on ONH
301   biomechanics by focusing on the plane behavior, (Voorhees et al., 2017a; Voorhees et al., 2017b)
302   this is a major simplification that likely has a substantial effect on stretch-induced ONH collagen
303   deformations. The approach used herein, however, does have one important positive aspect: the
304   collagen visible in the images is all there is in the sample. This is in contrast to the vast majority
305   of experiments of the posterior pole in which only part of the sample is visible. For example, in
306   inflation experiments it may be possible to measure deformations of the sclera surface, but any
307   mechanics within the tissues must be assumed or inferred. (Bruno et al., 2018; Geraghty et al.,
308   2020)

309   Third, ONH sections were stretched either uniaxially or biaxially. This loading condition is a
310   fairly common assumption in studies on ONH biomechanics when the intent is to simulate the
311   tension in the ONH induced by IOP. (Perez et al., 2014; Voorhees et al., 2017b; Zhang et al.,
312   2015) It remains to be determined whether the ONH collagen deformation identified in this study
313   extends to physiological loading conditions or not. Also, whilst it is fairly likely that the loading
314   applied to the scleral samples is not physiologic, the conditions may be more realistic for LC
315   beams. Because the neural tissues adjacent to the beams are substantially more compliant than
316   the beam, the assumptions of in-plane stretch along the beam may approximate the physiological
317   condition better.

318   Fourth, the orientation-encoded colors in IPOL are cyclic, *i.e.*, repeating every 90 degrees. As
319   a result, two fibers oriented perpendicularly to each other exhibit the same color. Based on color-
320   angle mapping, these two fibers would have the same quantified orientation angles. This may
321   affect the quantification of collagen fiber interweaving and large rotation of collagen fibers under

322   stretch, which was beyond the scope of this study. It is possible to modify the setup to create a

323   system repeating every 180 degrees. This, however, may adversely affect angular resolution.

324   Fifth, to capture the deformation of the entire ONH region under biaxial stretch, we stitched

325   multiple images into mosaics at each stretch level. Mosaicking is only suitable for imaging quasi-

326   static tissue deformation and may cause image artifacts such as imperfect registration, poor or

327   irregular focus, or inconsistent illumination. Implementing IPOL with a dissecting microscope with

328   a broader depth of field and a deeper focal depth can achieve a large field of view of a single

329   image and thus circumvents the need for mosaicking, potentially at the cost of resolving power.

330   (Lee et al., 2020)

331   In conclusion, we have demonstrated that IPOL allows visualization and quantification of

332   changes in ONH collagen morphology and architecture under dynamic loading. This study

333   represents an important step towards using a novel imaging modality to study ONH collagen

334   microstructure and biomechanics, which could help understand the role of collagen microstructure

335   in eye physiology, aging, and in biomechanics-related diseases, such as glaucoma and myopia.

Acknowledgements

Disclosures

341   Ziyi Zhu was at the University of Pittsburgh when he contributed to this work. He is now at

342   Amazon; Other authors have nothing to disclose.

343

References

Akagi, T., Hangai, M., Takayama, K., Nonaka, A., Ooto, S., Yoshimura, N., 2012. In vivo imaging of lamina cribrosa pores by adaptive optics scanning laser ophthalmoscopy. Investigative ophthalmology & visual science 53, 4111-4119.

Behkam, R., Kollech, H.G., Jana, A., Hill, A., Danford, F., Howerton, S., Ram, S., Rodríguez, J.J., Utzinger, U., Girkin, C.A., 2019. Racioethnic differences in the biomechanical response of the lamina cribrosa. Acta biomaterialia 88, 131-140.

Bianco, G., Bruno, L., Girkin, C.A., Fazio, M.A., 2020. Full-field displacement measurement of corneoscleral shells by combining multi-camera speckle interferometry with 3D shape reconstruction. Journal of the Mechanical Behavior of Biomedical Materials 103, 103560.

Billiar, K., Sacks, M., 1997. A method to quantify the fiber kinematics of planar tissues under biaxial stretch. Journal of biomechanics 30, 753-756.

Bowman, A.W., Azzalini, A., 1997. Applied smoothing techniques for data analysis: the kernel approach with S-Plus illustrations. OUP Oxford.

Brazile, B.L., Hua, Y., Jan, N.-J., Wallace, J., Gogola, A., Sigal, I.A., 2018. Thin lamina cribrosa beams have different collagen microstructure than thick beams. Investigative ophthalmology & visual science 59, 4653-4661.

Brooks, D.E., Arellano, E., Kubilis, P.S., Komaromy, A.M., 1998. Histomorphometry of the porcine scleral lamina cribrosa surface. Veterinary ophthalmology 1, 129-135.

Brown, D.J., Morishige, N., Neekhra, A., Minckler, D.S., Jester, J.V., 2007. Application of second harmonic imaging microscopy to assess structural changes in optic nerve head structure ex vivo. Journal of biomedical optics 12, 024029.

Bruno, L., Bianco, G., Fazio, M.A., 2018. A multi-camera speckle interferometer for dynamic full-field 3D displacement measurement: validation and inflation testing of a human eye sclera. Optics and Lasers in Engineering 107, 91-101.

Candia, O.A., Gerometta, R.M., Danias, J., 2014. Tissue plasminogen activator reduces the elevated intraocular pressure induced by prednisolone in sheep. Experimental eye research 128, 114-116.

Chung, C.W., Girard, M.J., Jan, N.-J., Sigal, I.A., 2016. Use and misuse of Laplace's law in ophthalmology. Investigative ophthalmology & visual science 57, 236-245.

Coudrillier, B., Boote, C., Quigley, H.A., Nguyen, T.D., 2013. Scleral anisotropy and its effects on the mechanical response of the optic nerve head. Biomechanics and modeling in mechanobiology 12, 941-963.

Coudrillier, B., Tian, J., Alexander, S., Myers, K.M., Quigley, H.A., Nguyen, T.D., 2012. Biomechanics of the human posterior sclera: age-and glaucoma-related changes measured using inflation testing. Investigative ophthalmology & visual science 53, 1714-1728.

Eilaghi, A., Flanagan, J.G., Tertinegg, I., Simmons, C.A., Brodland, G.W., Ethier, C.R., 2010. Biaxial mechanical testing of human sclera. Journal of biomechanics 43, 1696-1701.

Elkington, A., Inman, C., Steart, P., Weller, R., 1990. The structure of the lamina cribrosa of the human eye: an immunocytochemical and electron microscopical study. Eye 4, 42.

Ethier, C.R., Johnson, M., Ruberti, J., 2004a. Ocular biomechanics and biotransport. Annual Review of Biomedical Engineering 6, 249-273.

Ethier, C.R., Johnson, M., Ruberti, J., 2004b. Ocular biomechanics and biotransport. Annu. Rev. Biomed. Eng. 6, 249-273.

Fazio, M.A., Clark, M.E., Bruno, L., Girkin, C.A., 2018. In vivo optic nerve head mechanical response to intraocular and cerebrospinal fluid pressure: imaging protocol and quantification method. Scientific reports 8, 12639.

Fontana, L., Bhandari, A., Fitzke, F., Hitchings, R., 1998. In vivo morphometry of the lamina cribrosa and its relation to visual field loss in glaucoma. Current eye research 17, 363-369.

393 Geraghty, B., Abass, A., Eliasy, A., Jones, S.W., Rama, P., Kassem, W., Akhtar, R., Elsheikh, A.,
394   2020. Inflation experiments and inverse finite element modelling of posterior human sclera.
395   Journal of biomechanics 98, 109438.
396 Gerometta, R., Spiga, M.-G., Borrás, T., Candia, O.A., 2010. Treatment of sheep steroid–induced
397   ocular hypertension with a glucocorticoid-inducible MMP1 gene therapy virus. Investigative
398   ophthalmology & visual science 51, 3042-3048.
399 Girard, M.J., Dahlmann-Noor, A., Rayapureddi, S., Bechara, J.A., Bertin, B.M., Jones, H., Albon,
400   J., Khaw, P.T., Ethier, C.R., 2011. Quantitative mapping of scleral fiber orientation in normal
401   rat eyes. Invest Ophthalmol Vis Sci 52, 9684-9693.
402 Girard, M.J., Downs, J.C., Bottlang, M., Burgoyne, C.F., Suh, J.-K.F., 2009. Peripapillary and
403   posterior scleral mechanics—part II: experimental and inverse finite element
404   characterization. Journal of biomechanical engineering 131, 051012.
405 Gogola, A., Jan, N.-J., Brazile, B., Lam, P., Lathrop, K.L., Chan, K.C., Sigal, I.A., 2018a. Spatial
406   Patterns and Age-Related Changes of the Collagen Crimp in the Human Cornea and Sclera.
407   Investigative Ophthalmology & Visual Science 59, 2987-2998.
408 Gogola, A., Jan, N.-J., Lathrop, K.L., Sigal, I.A., 2018b. Radial and Circumferential Collagen
409   Fibers Are a Feature of the Peripapillary Sclera of Human, Monkey, Pig, Cow, Goat, and
410   Sheep. Investigative ophthalmology & visual science 59, 4763-4774.
411 Gruev, V., Perkins, R., York, T., 2010. CCD polarization imaging sensor with aluminum nanowire
412   optical filters. Optics express 18, 19087-19094.
413 Grytz, R., Meschke, G., 2009. Constitutive modeling of crimped collagen fibrils in soft tissues.
414   Journal of the mechanical behavior of biomedical materials 2, 522-533.
415 Grytz, R., Sigal, I.A., Ruberti, J.W., Meschke, G., Downs, J.C., 2012. Lamina cribrosa thickening
416   in early glaucoma predicted by a microstructure motivated growth and remodeling approach.
417   Mechanics of Materials 44, 99-109.
418 Hansen, K.A., Weiss, J.A., Barton, J.K., 2002. Recruitment of tendon crimp with applied tensile
419   strain. Journal of Biomechanical Engineering 124, 72-77.
420 Hill, M.R., Duan, X., Gibson, G.A., Watkins, S., Robertson, A.M., 2012. A theoretical and non-
421   destructive experimental approach for direct inclusion of measured collagen orientation and
422   recruitment into mechanical models of the artery wall. Journal of biomechanics 45, 762-771.
423 Ho, L.C., Sigal, I.A., Jan, N.-J., Squires, A., Tse, Z., Wu, E.X., Kim, S.-G., Schuman, J.S., Chan,
424   K.C., 2014. Magic angle–enhanced MRI of fibrous microstructures in sclera and cornea with
425   and without intraocular pressure loading. Investigative ophthalmology & visual science 55,
426   5662-5672.
427 Ho, L.C., Sigal, I.A., Jan, N.-J., Yang, X., Van Der Merwe, Y., Yu, Y., Chau, Y., Leung, C.K.,
428   Conner, I.P., Jin, T., 2016. Non-invasive MRI assessments of tissue microstructures and
429   macromolecules in the eye upon biomechanical or biochemical modulation. Scientific
430   reports 6, 32080.
431 Holzapfel, G.A., 2001. Biomechanics of soft tissue. The handbook of materials behavior models
432   3, 1049-1063.
433 Jan, N.-J., Brazile, B.L., Hu, D., Grube, G., Wallace, J., Gogola, A., Sigal, I.A., 2018. Crimp around
434   the globe; patterns of collagen crimp across the corneoscleral shell. Experimental eye
435   research 172, 159-170.
436 Jan, N.-J., Gomez, C., Moed, S., Voorhees, A.P., Schuman, J.S., Bilonick, R.A., Sigal, I.A., 2017a.
437   Microstructural crimp of the lamina cribrosa and peripapillary sclera collagen fibers.
438   Investigative ophthalmology & visual science 58, 3378-3388.
439 Jan, N.-J., Sigal, I.A., 2018. Collagen fiber recruitment: a microstructural basis for the nonlinear
440   response of the posterior pole of the eye to increases in intraocular pressure. Acta
441   biomaterialia 72, 295-305.

442   Jan, N.J., Grimm, J.L., Tran, H., Lathrop, K.L., Wollstein, G., Bilonick, R.A., Ishikawa, H.,
443   Kagemann, L., Schuman, J.S., Sigal, I.A., 2015. Polarization microscopy for characterizing
444   fiber orientation of ocular tissues. Biomed Opt Express 6, 4705-4718.
445   Jan, N.J., Lathrop, K., Sigal, I.A., 2017b. Collagen Architecture of the Posterior Pole: High-
446   Resolution Wide Field of View Visualization and Analysis Using Polarized Light Microscopy.
447   Invest Ophthalmol Vis Sci 58, 735-744.
448   Kang, M.H., Yu, D.-Y., 2015. Distribution pattern of axonal cytoskeleton proteins in the human
449   optic nerve head. Neural regeneration research 10, 1198.
450   Lee, P.-Y., Yang, B., Hua, Y., Brazile, B., Ji, F., Zhu, Z., Fryc, G.A., Sigal, I.A., 2020. Instant
451   polarized light microscopy for real-time wide-field visualization of collagen architecture,
452   Label-free Biomedical Imaging and Sensing (LBIS) 2020. International Society for Optics
453   and Photonics, p. 112510Y.
454   Lee, P.-Y., Yang, B., Sigal, I.A., 2019a. Real-time measurement of collagen architecture and
455   deformations at sub-micron resolution, Summer Biomechanics, Bioengineering, and
456   Biotransport Conference, Seven Springs, PA, USA.
457   Lee, P., Yang, B., Sigal, I., 2019b. Real-time measurement of collagen architecture and
458   deformations at sub-micron resolution, Summer Biomechanics, Bioengineering, and
459   Biotransport Conference.
460   Ling, Y.T.T., Shi, R., Midgett, D.E., Jefferys, J.L., Quigley, H.A., Nguyen, T.D., 2019.
461   Characterizing the Collagen Network Structure and Pressure-Induced Strains of the Human
462   Lamina Cribrosa. Invest Ophthalmol Vis Sci 60, 2406-2422.
463   Ma, Y., Pavlatos, E., Clayson, K., Kwok, S., Pan, X., Liu, J., 2020. Three-dimensional inflation
464   response of porcine optic nerve head using high-frequency ultrasound elastography.
465   Journal of Biomechanical Engineering 142, 051013.
466   Ma, Y., Pavlatos, E., Clayson, K., Pan, X., Kwok, S., Sandwisch, T., Liu, J., 2019. Mechanical
467   deformation of human optic nerve head and peripapillary tissue in response to acute IOP
468   elevation. Investigative ophthalmology & visual science 60, 913-920.
469   Masters, B.R., 1998. Three-dimensional confocal microscopy of the human optic nerve in vivo.
470   Optics Express 3, 356-359.
471   Midgett, D.E., Quigley, H.A., Nguyen, T.D., 2019. In vivo characterization of the deformation of
472   the human optic nerve head using optical coherence tomography and digital volume
473   correlation. Acta biomaterialia 96, 385-399.
474   Miller, K.M., Quigley, H.A., 1988. The clinical appearance of the lamina cribrosa as a function of
475   the extent of glaucomatous optic nerve damage. Ophthalmology 95, 135-138.
476   Pavlatos, E., Ma, Y., Clayson, K., Pan, X., Liu, J., 2018. Regional deformation of the optic nerve
477   head and peripapillary sclera during IOP elevation. Investigative ophthalmology & visual
478   science 59, 3779-3788.
479   Pavlatos, E., Perez, B.C., Morris, H.J., Chen, H., Palko, J.R., Pan, X., Weber, P.A., Hart, R.T.,
480   Liu, J., 2016. Three-dimensional strains in human posterior sclera using ultrasound speckle
481   tracking. Journal of biomechanical engineering 138, 021015.
482   Perez, B.C., Tang, J., Morris, H.J., Palko, J.R., Pan, X., Hart, R.T., Liu, J., 2014. Biaxial
483   mechanical testing of posterior sclera using high-resolution ultrasound speckle tracking for
484   strain measurements. Journal of biomechanics 47, 1151-1156.
485   Qian, X., Kang, H., Li, R., Lu, G., Du, Z., Shung, K.K., Humayun, M.S., Zhou, Q., 2020. In vivo
486   Visualization of Eye Vasculature using Super-resolution Ultrasound Microvessel Imaging.
487   IEEE Transactions on Biomedical Engineering.
488   Quantock, A.J., Winkler, M., Parfitt, G.J., Young, R.D., Brown, D.J., Boote, C., Jester, J.V., 2015.
489   From nano to macro: studying the hierarchical structure of the corneal extracellular matrix.
490   Experimental eye research 133, 81-99.

Quigley, H.A., Addicks, E.M., 1981. Regional differences in the structure of the lamina cribrosa and their relation to glaucomatous optic nerve damage. Archives of ophthalmology 99, 137-143.

Quigley, H.A., Hohman, R.M., Addicks, E.M., Massof, R.W., Green, W.R., 1983. Morphologic changes in the lamina cribrosa correlated with neural loss in open-angle glaucoma. American journal of ophthalmology 95, 673-691.

Schindelin, J., Arganda-Carreras, I., Frise, E., Kaynig, V., Longair, M., Pietzsch, T., Preibisch, S., Rueden, C., Saalfeld, S., Schmid, B., 2012. Fiji: an open-source platform for biological-image analysis. Nature methods 9, 676-682.

Schuman, J.S., Kostanyan, T., Bussel, I., 2020. Review of longitudinal glaucoma progression: 5 years after the shaffer lecture. Ophthalmology Glaucoma 3, 158-166.

Sigal, I.A., Flanagan, J.G., Tertinegg, I., Ethier, C.R., 2007. Predicted extension, compression and shearing of optic nerve head tissues. Experimental eye research 85, 312-322.

Sigal, I.A., Grimm, J.L., Jan, N.J., Reid, K., Minckler, D.S., Brown, D.J., 2014a. Eye-specific IOP-induced displacements and deformations of human lamina cribrosa. Invest Ophthalmol Vis Sci 55, 1-15.

Sigal, I.A., Wang, B., Strouthidis, N.G., Akagi, T., Girard, M.J., 2014b. Recent advances in OCT imaging of the lamina cribrosa. British Journal of Ophthalmology 98, ii34-ii39.

Thornton, G., Shrive, N., Frank, C., 2002. Ligament creep recruits fibres at low stresses and can lead to modulus-reducing fibre damage at higher creep stresses: a study in rabbit medial collateral ligament model. Journal of Orthopaedic Research 20, 967-974.

Tower, T.T., Neidert, M.R., Tranquillo, R.T., 2002. Fiber alignment imaging during mechanical testing of soft tissues. Annals of biomedical engineering 30, 1221-1233.

Voorhees, A.P., Jan, N.-J., Hua, Y., Yang, B., Sigal, I.A., 2018. Peripapillary sclera architecture revisited: a tangential fiber model and its biomechanical implications. Acta biomaterialia 79, 113-122.

Voorhees, A.P., Jan, N.J., Austin, M.E., Flanagan, J.G., Sivak, J.M., Bilonick, R.A., Sigal, I.A., 2017a. Lamina Cribrosa Pore Shape and Size as Predictors of Neural Tissue Mechanical Insult. Invest Ophthalmol Vis Sci 58, 5336-5346.

Voorhees, A.P., Jan, N.J., Sigal, I.A., 2017b. Effects of collagen microstructure and material properties on the deformation of the neural tissues of the lamina cribrosa. Acta Biomater 58, 278-290.

Wang, B., Hua, Y., Brazile, B.L., Yang, B., Sigal, I.A., 2020. Collagen fiber interweaving is central to sclera stiffness. Acta Biomaterialia, In Press.

Wang, B., Nevins, J.E., Nadler, Z., Wollstein, G., Ishikawa, H., Bilonick, R.A., Kagemann, L., Sigal, I.A., Grulkowski, I., Liu, J.J., 2013. In vivo lamina cribrosa micro-architecture in healthy and glaucomatous eyes as assessed by optical coherence tomography. Investigative ophthalmology & visual science 54, 8270-8274.

Wei, J., Yang, B., Voorhees, A.P., Tran, H., Brazile, B., Wang, B., Schuman, J., Smith, M.A., Wollstein, G., Sigal, I.A., 2018. Measuring in-vivo and in-situ ex-vivo the 3D deformation of the lamina cribrosa microstructure under elevated intraocular pressure, Optical Elastography and Tissue Biomechanics V. International Society for Optics and Photonics, p. 1049611.

Weik, M.H., 2001. Full-width at half-maximum, Computer Science and Communications Dictionary. Springer US, Boston, MA, pp. 661-661.

Yan, D., McPheeters, S., Johnson, G., Utzinger, U., Geest, J.P.V., 2011. Microstructural differences in the human posterior sclera as a function of age and race. Investigative ophthalmology & visual science 52, 821-829.

Yang, B., Brazile, B., Jan, N.-J., Hua, Y., Wei, J., Sigal, I.A., 2018a. Structured polarized light microscopy for collagen fiber structure and orientation quantification in thick ocular tissues. Journal of biomedical optics 23, 106001.

542 Yang, B., Jan, N.J., Brazile, B., Voorhees, A., Lathrop, K.L., Sigal, I.A., 2018b. Polarized light
543   microscopy for 3-dimensional mapping of collagen fiber architecture in ocular tissues.
544   Journal of biophotonics 11, e201700356.
545 Yang, B., Lee, P.-Y., Brazile, B., Sigal, I.A., 2019. Snapshot-polarized light microscopy to visualize
546   and quantify collagenous soft tissue microstructure at 156 frames/second, SB3C - Summer
547   Biomechanics, Bioengineering and Biotransport Conference, Seven Springs, PA.
548 Yang, B., Lee, P.Y., Hua, Y., Brazile, B., Waxman, S., Ji, F., Zhu, Z., Sigal, I.A., 2021. Instant
549   polarized light microscopy for imaging collagen microarchitecture and dynamics. Journal of
550   Biophotonics 14, e202000326.
551 York, T., Kahan, L., Lake, S.P., Gruev, V., 2014. Real-time high-resolution measurement of
552   collagen alignment in dynamically loaded soft tissue. Journal of biomedical optics 19,
553   066011.
554 Zhang, L., Albon, J., Jones, H., Gouget, C.L., Ethier, C.R., Goh, J.C., Girard, M.J., 2015. Collagen
555   microstructural factors influencing optic nerve head biomechanics. Investigative
556   ophthalmology & visual science 56, 2031-2042.
557 Zwillinger, S., Paques, M., Safran, B., Baudouin, C., 2016. In vivo characterization of lamina
558   cribrosa pore morphology in primary open-angle glaucoma. Journal Français
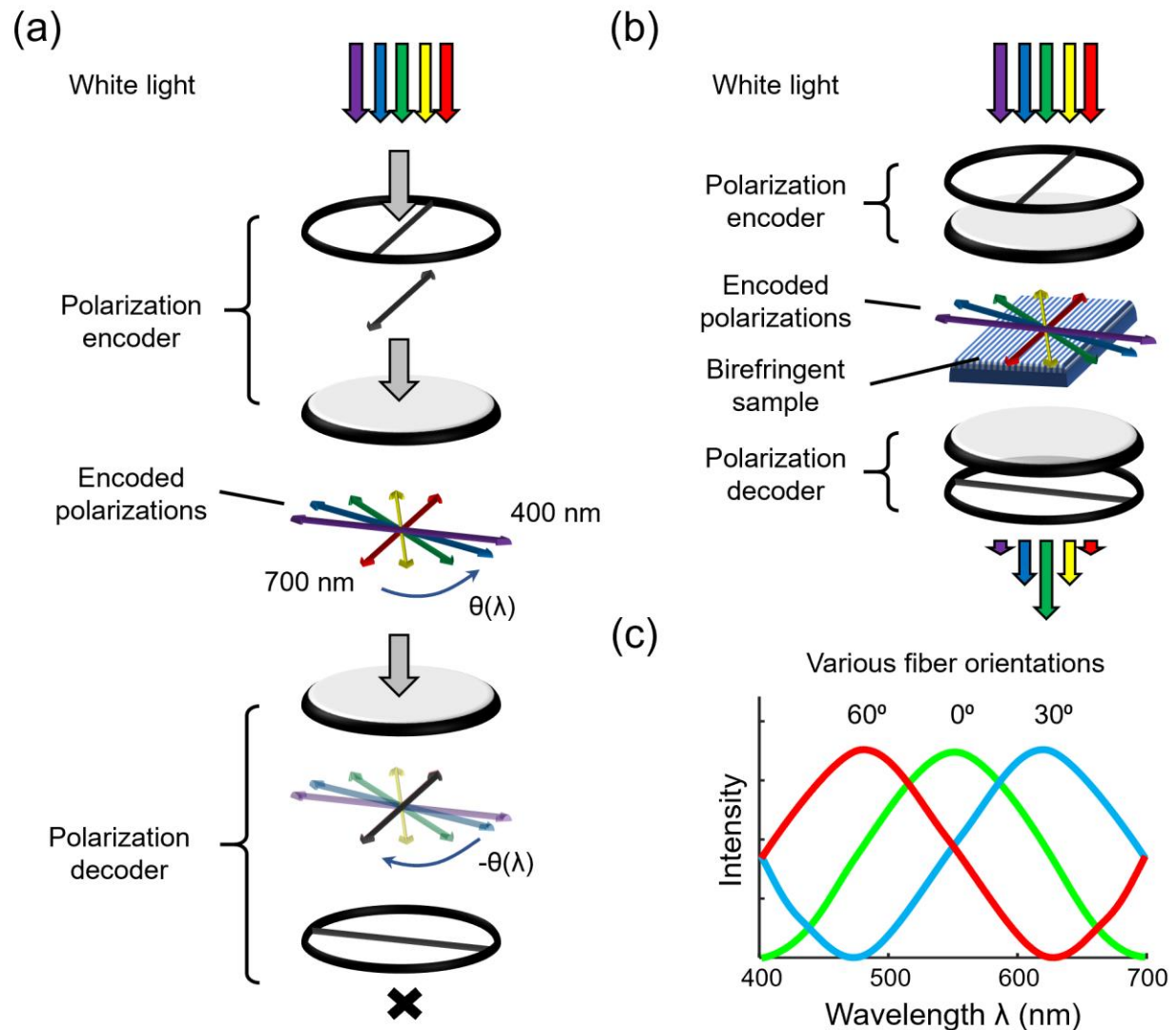559   D'Ophtalmologie 39, 265-271.
560

561

Figure 1. Schematic diagram of IPOL imaging system. **(a)** The white light passing through the polarization encoder was linearly polarized. The polarization directions of the spectrum were diverged within 90 degrees. In the absence of a birefringent sample, the polarization decoder did not allow light to pass through the system. **(b)** As the encoded polarized light passed through a birefringent sample, such as collagen, the aspect ratio of polarization of each wavelength was modulated based on the collagen fiber orientation. A new spectrum was then generated after the modulated polarized light passed through the polarization decoder. **(c)** The colorful light was acquired by a color camera to produce true-color images indicating collagen fiber orientation.
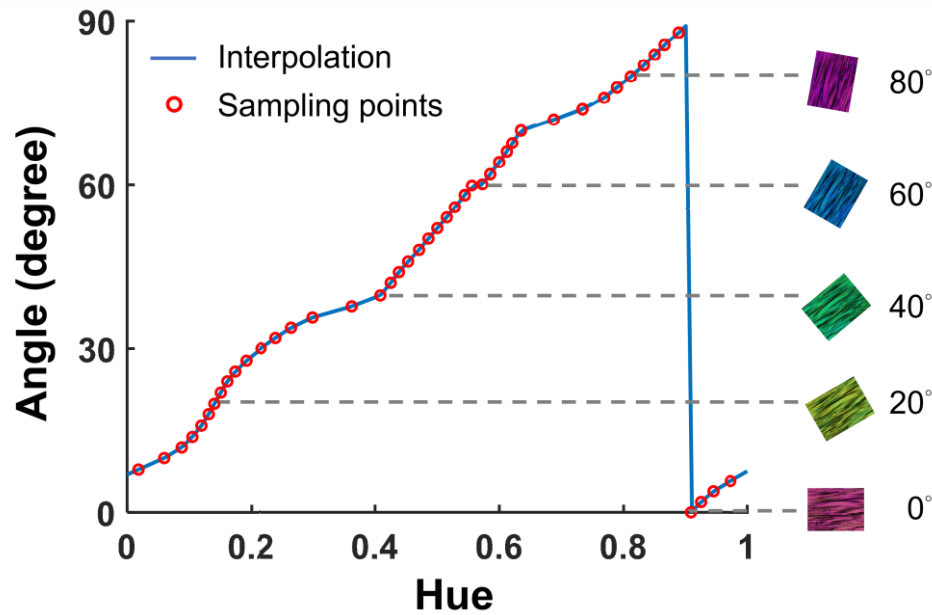
Figure 2. IPOL calibration curve. The curve was obtained from the circular interpolation of fiber orientation as a function of hue (*i.e.*, the parameter of a color as determined by its dominant wavelength). Shown on the right are five example IPOL images of the same chicken tendon section at known orientations. Details of the calibration are described elsewhere. (Yang et al., 2021)
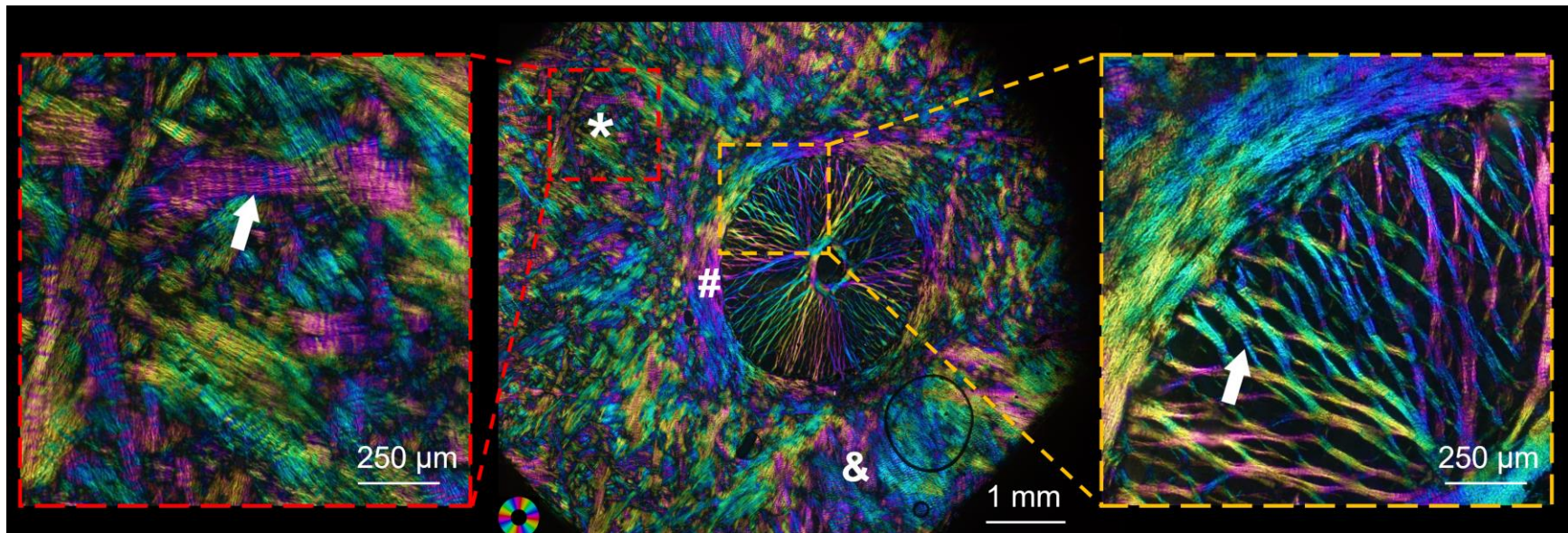
Figure 3. An IPOL image that was a mosaic acquired of a static coronal section from the ONH of a fresh sheep eye. Color in the image represents local fiber orientation and density. The black rings are optical artifacts due to air bubbles. In the PPS, there were fibers aligned circumferentially around the canal (#), fibers oriented radially from the canal (&), and unaligned interweaving fibers (*). In the LC, intersecting fibers formed large knots and wrapped around neural tissue pores, with beam insertions into the scleral canal wall that were either narrow and straight or wide and flared. Close-up shows fiber interweaving in the PPS (red box) and intersecting beams in the LC (yellow box). Crimp, or the natural waviness of collagen fibers is clearly discernible (marked by the white arrows; undulations in color).
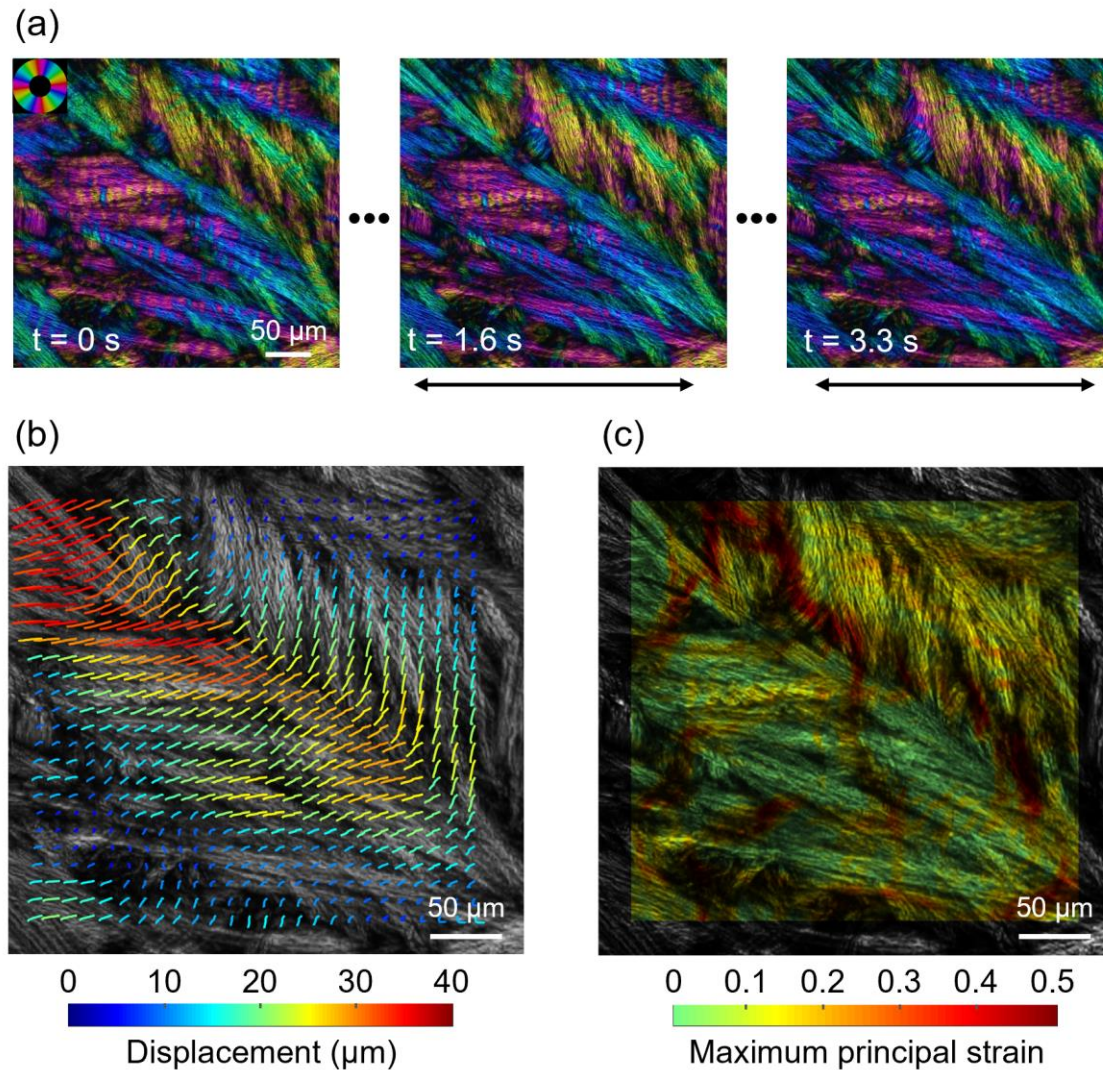
Figure 4. IPOL can capture highly dynamic deformations of ocular tissues in detail. **(a)** Time-sequence IPOL images of the PPS under uniaxial stretch. The black arrows indicate the stretch direction. 100 images were captured within 3.3 s. We show three images here to indicate the initial (t = 0 s), middle (t = 1.6 s), and final (t = 3.3 s) states. **(b)** Traces of stretch-induced tissue displacement. The motion trails were tortuous and anisotropic. For better visualization of tissue displacement, the color IPOL image was transformed into the grayscale image. **(c)** Contour plot of the maximum principal strain. Despite the PPS was under uniaxial stretch, its deformation was non-affine, *i.e.*, the local deformation differs from the applied stretch. High strains were mainly located at fibers oriented transversely to the stretch direction. The peak strain reached 50%. It is important to note that these deformations were obtained in a well-controlled stretch test, which are likely different from in vivo or in situ, but that nevertheless provide a valuable opportunity to study the inter-relationship of structure and mechanics in ocular tissues.
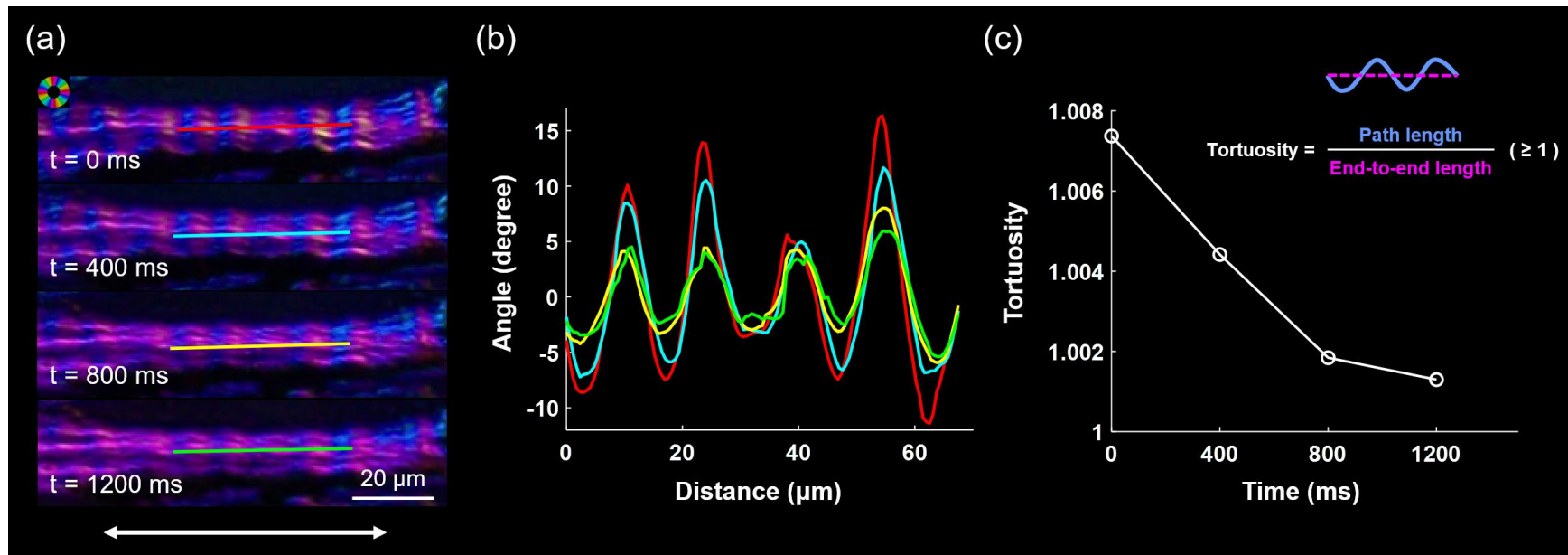
Figure 5. Uncrimping process of an LC beam under uniaxial stretch. **(a)** IPOL images of an LC beam captured at four time points with an interval of 400 ms. The white arrows indicate the stretch direction. Before stretch (t = 0 ms), the beam was crimped, as evidenced by color undulations along the beam, without torsion. As the stretch increased, there were less undulations in color, suggesting a reduction of crimp. **(b)** Fiber orientation profiles along the solid lines in (a), with colors corresponding to different time points. Before stretch, the orientation profile (red curve) exhibited periodicity with angles alternating between -10 and 15 degrees. As the stretch increased, the amplitude of the orientation profile decreased, indicating collagen uncrimping. Based on the difference in the period of the orientation profiles between the initial (red curve) and final (green curve) states, the stretch of the LC beam was measured as 3.6%. At this stretch level, the LC beam did not reach full uncrimping. **(c)** The high spatial and angular details allow measurement of crimp tortuosity along the beam. As expected, the tortuosity or degree of undulation, decreases with time and stretch.
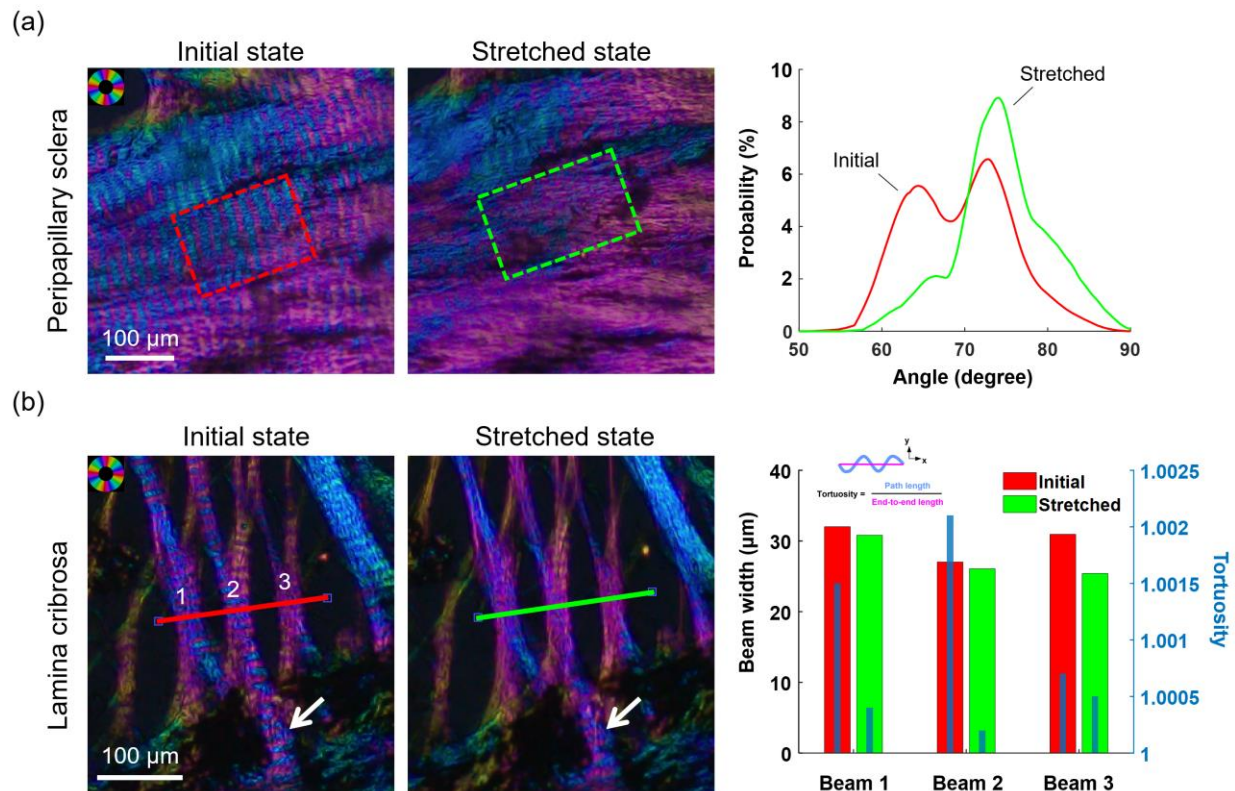
Figure 6. PPS and LC fiber uncrimping under biaxial stretch. **(a)** IPOL images of the PPS at the initial and stretched states. To quantify stretch-induced changes in collagen crimp, angle distributions were measured within a region of interest (ROI, dashed rectangle) and compared before and after stretch. At the initial state, the angle distribution within the ROI exhibited a bimodal pattern, indicating crimped fibers. In the stretched state, the distribution changed into a unimodal pattern due to uncrimping. **(b)** IPOL images of the LC at the initial and stretched states. We measured the crimp tortuosity and width (along the dashed line) of three beams. Before stretch, the tortuosity of Beams 1, 2, and 3 was 1.0032, 1.0048, and 1.0011, and their width was 32, 27, and 31 µm, respectively. After stretch, both the tortuosity and width of the three beams decreased. The tortuosity decreased by 72%, 69%, and 46%, and the width decreased by 3.8%, 3.5%, and 18%, respectively. Beam 3, which was less crimped (*i.e.*, smaller tortuosity) than Beams 1 and 2 before stretch, narrowed more after stretch.
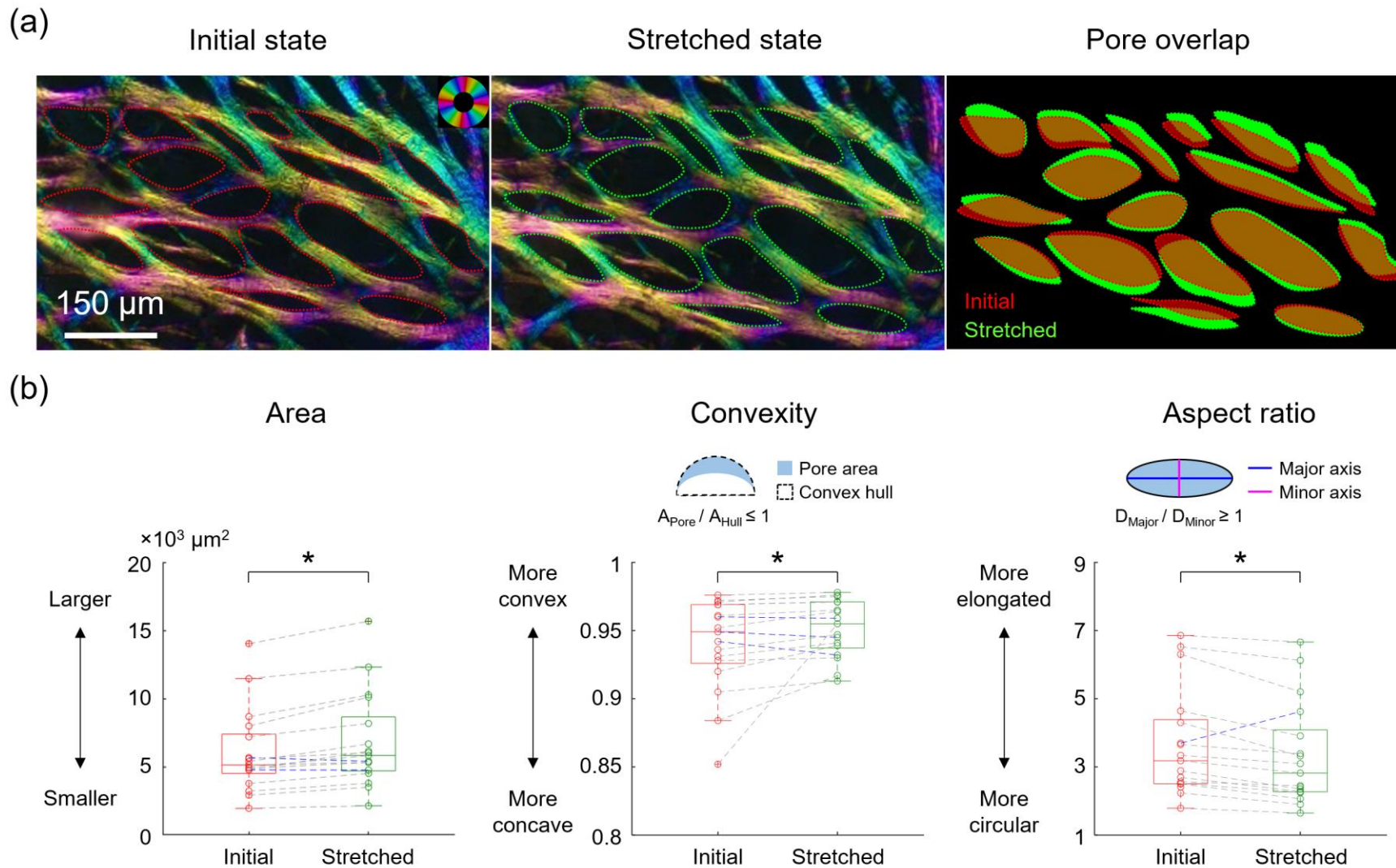
Figure 7. Deformation of LC pores under biaxial stretch. **(a)** 17 pores were traced at the initial and stretched states, and then overlaid to show the differences in pore contour shape and size before and after stretch. The overlapped image shows that stretch-induced pore deformation was anisotropic within a single pore and non-uniform among pores, indicating that neural tissues and vessels within

625 pores suffer shear deformation. **(b)** Box plots of area, convexity, and aspect ratio of the 17 pores at the initial and stretched states. The

626 dotted lines in the box plots connect the data points corresponding to the same pore at the initial and stretched states, where the blue

627 dotted lines represent the opposite trend against the majority of the pore changes. After stretch, 15 and 14 pores have increases in

628 pore area and convexity, respectively, and 16 pores have a decrease in pore aspect ratio; the average pore area and convexity

629 increased by 13% and 1.3%, respectively, and the average pore aspect ratio decreased by 9%. This suggests that pores became

630 larger, more convex, and more circular after stretch. Convexity was defined as the ratio of the area of the pore to the area of the convex

631 hull of the pore. Aspect ratio was defined as the ratio of the major axis length to the minor axis length. The superscript * indicates $P <$
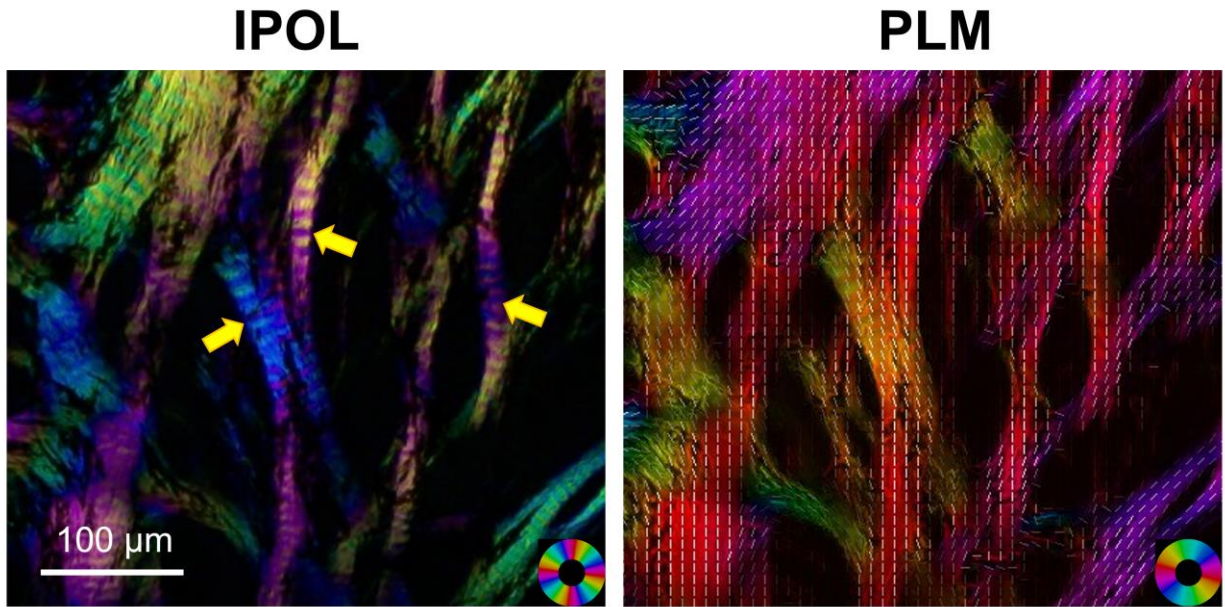
632 0.05.

Figure 8. A comparison between the IPOL (left) and PLM (right) images of a sheep ONH section. The collagen crimp of the LC beams (yellow arrows) is easily discernible in the IPOL image due to its high spatial and angular resolutions. Note that the orientation-encoded colors repeat every 90 degrees in IPOL and every 180 degrees in PLM. The white lines in the PLM image represent local fiber orientations.